Numerical investigation on plasma and poly-Si etching uniformity control over a large area in a resonant inductively coupled plasma source

Cite as: Physics of Plasmas **8**, 1384 (2001); https://doi.org/10.1063/1.1350671
Submitted: 22 August 2000 . Accepted: 21 December 2000 . Published Online: 22 March 2001

S. S. Kim, S. Hamaguchi, N. S. Yoon, C. S. Chang, Y. D. Lee, and S. H. Ku

Numerical investigation on plasma and poly-Si etching uniformity control over a large area in a resonant inductively coupled plasma source

S. S. Kim[a] and S. Hamaguchi
Department of Fundamental Energy Science, Graduate School of Energy Science, Kyoto University, Uji, Kyoto, Japan 611-0011

N. S. Yoon
School of Electrical and Electronics Engineering, Chungbuk National University, Cheongju, Korea 361-480

C. S. Chang, Y. D. Lee, and S. H. Ku
Department of Physics, Korea Advanced Institute of Science and Technology, Taejon, Korea 305-701

(Received 22 August 2000; accepted 21 December 2000)

In high-density plasma etching processes for ultra-large-scale integrated (ULSI) circuits, the uniformity of the plasma over a large area is of major concern. Recently a resonant inductively coupled plasma source [S. S. Kim *et al.*, Appl. Phys. Lett. **77**, 492 (2000)] has been proposed for large-area plasma processing, which achieves large-area plasma uniformity by properly tuning its antenna with an external variable capacitor. In the present paper, the plasma transport and poly-Si etching characteristics of this plasma source have been numerically investigated using a self-consistent model for electron heating, plasma transport, and microscopic etching profiles. The numerical simulation results indicate that uniform poly-Si etching over 300 mm in diameter can be easily achieved in this plasma source. © *2001 American Institute of Physics.*
[DOI: 10.1063/1.1350671]

I. INTRODUCTION

High density plasma sources, such as those employing inductively coupled plasmas (ICPs), electron cyclotron resonance (ECR) plasmas, and helicon wave plasmas, are currently used for 200 mm wafer etching processes. However, scaling-up of these plasma sources for the next-generation 300 mm wafer processes is not straightforward due to the increase of antenna inductances and complexity of components, such as magnetic coils and wave guides. Recently, various discharge sources for large-area processing have been proposed, including inductively coupled plasma sources with multiple inductive antennas[1] or with antennas that launch traveling waves,[2] ECR plasma sources with plane slotted antennas and permanent magnets,[3] modified magnetron-typed radio-frequency (rf) plasma sources,[4] or ultra-high-frequency (UHF) plasma sources with spokewise antennas.[5]

Recently Kim *et al.* has proposed a new antenna configuration to produce uniform large-area ICPs,[6] using the parallel LC-resonance of the antenna (Resonant ICP or RICP). The antenna of this system consists of segmented coils, which are connected in parallel and tuned with an external variable capacitor as shown in Fig. 1(a). The LC-resonance induced by the external capacitor increases outer-coil currents, generating higher-density plasmas in the peripheral region to obtain uniform plasmas over large area.[6] The variable capacitance therefore serves as an adjustable parameter to control the plasma uniformity.

To date, much work has been done on fundamental ICP discharge physics[7–11] and theoretical models.[12–17] However, development of self-consistent fluid models for ICP discharges has been slow due to the lack of two-dimensional general heating formulas and the numerical instability caused by the dielectric relaxation time. The main difficulty in developing a two-dimensional electron heating model arises from the fact that the radial normal mode of an electron kinetic equation is not compatible with the eigenmode of the wave equation.[18] The recently developed two-dimensional nonlocal heating theory[18] has overcome this problem in the case where the radius of the reactor chamber is sufficiently larger than the skin depth. This condition is met for large-area ICPs.

In this paper, we shall present numerical simulation results of plasma transport and polycrystalline-silicon etching characteristics of the large-area RICP source described by Kim *et al.*[6] mentioned above. For the numerical simulations, we have developed a self-consistent fluid model for electron heating, plasma transport, and etch profiles, based on which new simulation codes have been developed. For the electron heating, we have employed the model based on the nonlocal theory by Yoon *et al.*[18] We have also developed a new numerical scheme to solve fluid equations that is limited by the dielectric relaxation time.[19]

In our simulations, the fluid simulation module is combined with the electron heating module in a self-consistent manner, and the results obtained from these modules are used as input data of the etching simulation module, as shown schematically in Fig. 2. Using these simulations, we shall show that the radial uniformity of Ar and Cl_2 plasmas can be controlled by varying the external capacitance to yield uniform poly-Si etching over 300 mm in diameter.

[a]Also at: Korea Basic Science Institute, Taejon, Korea 305-333.

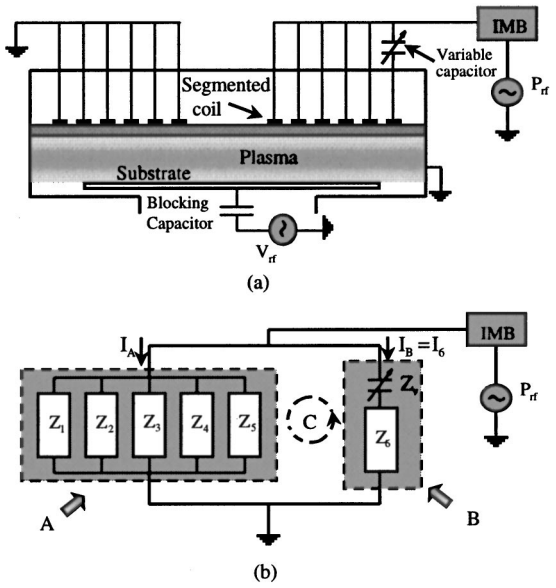

FIG. 1. Schematic diagram of (a) a large-area ICP source with an antenna composed of segmented coils and an external variable capacitor and (b) its equivalent circuit.

The rest of the paper is organized as follows. In Sec. II, we shall briefly introduce the antenna configuration of the large-area RICP source. The models for electron heating, plasma transport, and etching simulation are described in Sec. III. The numerical results and discussions are presented in Sec. IV, and finally a concluding remark is given in Sec. V.

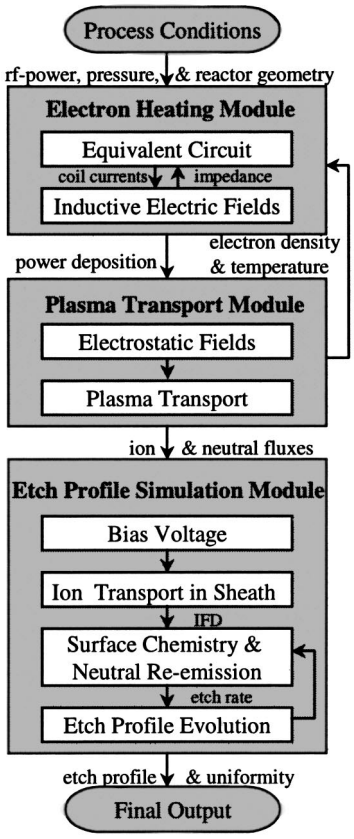

FIG. 2. Schematic diagram of the simulation modules.

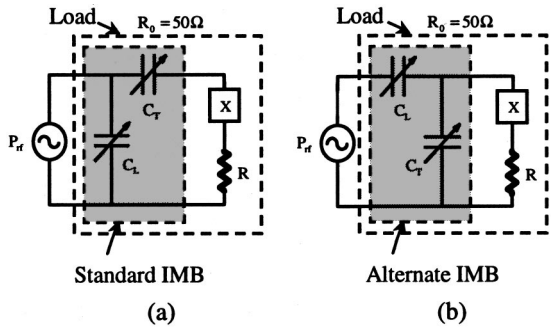

FIG. 3. Schematic diagram of (a) standard-type and (b) alternate-type impedance matching circuit. Here C_T and C_L mean tuning and loading capacitors, respectively.

II. NEW ANTENNA CONFIGURATION FOR LARGE-AREA ICP PROCESSING

A schematic illustration of the antenna configuration for the RICP is shown in Fig. 1(a). The antenna is powered from a rf-power supply through impedance matching box (IMB) which consists of two capacitors, i.e., tuning and loading capacitors, as shown in Fig. 3. The antenna used in this study consists of six-turn segmented coils which are connected in parallel. The segmentation and parallel connection of the coil system allow the system to have a low inductance, unlike the conventional multiturn spiral coil antenna. It is known that a large antenna inductance can cause unstable impedance matching and large antenna voltage, the latter causing the antenna to be capacitively coupled with the plasma resulting in low efficiency and nonuniform plasma production. The calculated absolute impedance values for our geometric configuration are $Z_{\text{spiral}} \simeq 605\,\Omega$ for a spiral antenna and $Z_{\text{seg}} \simeq 8\,\Omega$ for the segmented antenna. However, the segmented coil system can make the inner coils have a small inductance compared with outer coils and therefore can induce large inner coil currents, which may produce a radially nonuniform plasma. To avoid this problem, one of the segmented coils is connected with an external variable capacitor in series [see the outermost coil in Fig. 1(a)]. As will be shown, this variable capacitor serves as an external controller for the antenna current distribution and for plasma uniformity.

The equivalent circuit diagram for the system is shown in Fig. 1(b). In Fig. 1(b), Z_j $(j=1-6)$ denotes the lumped impedance of the jth coil in the presence of a plasma and Z_v is the impedance of the variable capacitor. The current in the circuit element, A, is given by $I_A = \Sigma_{j=1}^{5} I_j$, with I_j being the jth coil current, and $I_B = I_6$ is the current in the circuit element B. The currents will be determined by the LC-resonance induced in circuit C (i.e., the series connection of A and B), if the reactance of the circuit C is equal to zero. At the resonance condition, I_A is nearly equal to I_B, i.e., a large current is allowed to flow in the outer most coil. This large antenna current in the outer most coil generates more plasmas on the peripheral region of the chamber, where the plasma otherwise would have the lowest density.

III. MODEL DESCRIPTIONS

The model and simulation modules developed in this study are schematically described in Fig. 2. Power deposition into the plasma is calculated by the heating module, which consists of modules for the equivalent circuit and the inductive electric field which determine antenna coil currents, system impedance, and induced fields. The resulting power deposition profile is used to calculate the electron temperature in the plasma transport module. The plasma transport module then returns the space-averaged electron temperature and density to the heating module. These processes are repeated until a self-consistent steady state is obtained. The steady state values of ion and neutral fluxes obtained in these manners are then used as input parameters for the calculation of etch rates and profiles in the etch profile simulation module. The models used in each simulation module are described below.

A. Electron heating model

In order to determine inductive electric fields generated by the antenna given in Fig. 1(b) and the power deposition into the plasma, we have used a recently developed and analytic model of planar-type ICP based on collisionless nonlocal electron heating.[18,20,21] Using the analytic results in Refs. 18, 20, and 21 and the complex Poynting theorem,[22] we obtain the terminal voltage of the ith coil as follows:

$$V_i = -\frac{1}{I_i^*}\int_{\Omega_i} J_c^* \; E_\theta \; d^3x + R_{ci} I_i + \delta_{6i} Z_v I_i = \sum_{j=1}^{6} (\mathcal{Z}_{ij} + \delta_{6j} Z_v) I_j , \tag{1}$$

where I_i is the ith coil current, $*$ denotes the complex conjugate, Ω_i is the volume of the ith coil, J_c is the azimuthal coil current density, E_θ is the azimuthal inductive electric field, R_{ci} is the resistance of the ith coil, $\delta_{ij}=1$ (if $i=j$) or 0 (otherwise), and

$$\mathcal{Z}_{ij} = -\frac{4\pi^2 i\kappa}{c r_{\rm ch}^2}\sum_{m=1}^{\infty} \beta_m^{-3} J_2^{-2}(\alpha_{1m})[C_{mi}\{C_{mj}(Q_{mij}-P_{mij}) + B_{mj}H_{mij}\} + (B_{mj}/2)\{A_{mi}+(\beta_m \Delta z_i)B_{mi}-C_{mi}\}] + \delta_{ij}R_{ci} \tag{2}$$

represents the impedance, including mutual inductance, between the ith and jth coils, the coil resistance, and plasma impedance (the lumped impedance of the ith coil in the presence of the plasma is then given by $Z_i = \Sigma_{j=1}^{6} I_i^{-1}\mathcal{Z}_{ij} I_j$). Here,

$$\begin{aligned}
C_{mi} &= A_{mi}\cosh(\beta_m \Delta z_i/2) + B_{mi}\sinh(\beta_m \Delta z_i/2),\\
A_{mi} &= \frac{2\beta_m}{(\Delta r_i + \Delta z_i)}\int_{r_{i,1}}^{r_{i,2}} r J_1(\alpha_{1m} r/r_{ch})\,dr,\\
B_{mi} &= 2[r_{i,2}J_1(\alpha_{1m}r_{i,2}/r_{ch}) + r_{i,1}J_1(\alpha_{1m}r_{i,1}/r_{ch})]/(\Delta r_i + \Delta z_i),\\
Q_{mij} &= \cosh(\beta_m z_i)\cosh(\beta_m z_j)\tanh(\beta_m L_s) + \sinh(\beta_m(z_i+z_j))/2 - \cosh(\beta_m(z_i-z_j)) \times \tanh(\beta_m \Delta z_j/2)/2,\\
P_{mij} &= 2\sinh(\beta_m(z_i+L_s))\sinh(\beta_m(z_j+L_s)) \times \operatorname{csch}(2\beta_m L_s)\hat{b}_m ,\\
H_{mij} &= [1-\cosh(\beta_m(z_i-z_j))\operatorname{sech}(\beta_m \Delta z_j/2)]/2,\\
\hat{b}_m &= [1+(2\beta_m l^2/L)\coth(\beta_m L_s)S_m]^{-1},\\
S_m &= (\xi_{1m}^2 - \xi_{2m}^2)/\xi_{1m} .
\end{aligned} \tag{3}$$

In the above equations, $\kappa=\omega/c$ is the vacuum wave number, ω is the angular driving rf-frequency, $r_{\rm ch}$ and L are the chamber radius and height, Δr_i, Δz_i, $r_{i,1}$, $r_{i,2}$, and z_i are the width, thickness, inner radius, outer radius, and the axially central position of the ith coil, respectively. Also L_s denotes the shielding cap length, J_2 denotes the Bessel function of the second order, $\beta_m = \sqrt{(\alpha_{1m}/r_{\rm ch})^2 - \kappa^2}$ with α_{1m} being the mth zero of the Bessel function of the first order, $l = v_{\rm th}/\sqrt{\omega^2+\nu_{en}^2}$ is the effective mean free path of electrons, $v_{\rm th} = \sqrt{2T_e/m_e}$ is the electron thermal speed, $\nu_{en} = \Sigma_j N_j \int_0^\infty f(\epsilon)(2\epsilon/m)^{1/2}\sigma_{{\rm el},j}(\epsilon)\,d\epsilon$ is the electron-neutral collision frequency, N_j is the jth neutral species density, $\sigma_{{\rm el},j}$ is the elastic collision cross section between the electron and jth neutral species, whose values can be found in Ref. 12 for electron-Ar scattering and Ref. 23 for electron-Cl_2 or Cl scattering, $f(\epsilon)$ is the electron energy distribution function, which is assumed as a Maxwellian, $\xi_{1m} = 1/(2D_{m0}) + \Sigma_{n=1}^{\infty} 1/D_{mn}$, and $\xi_{2m} = 1/(2D_{m0}) + \Sigma_{n=1}^{\infty}(-1)^n/D_{mn}$, and

$$D_{mn} = \begin{cases} h_m^2 + \dfrac{\Lambda}{s} & (\text{for } n=0),\\[2ex] h_m^2 + k_n^2 - \dfrac{\Lambda}{k_n} Z_p\!\left(\dfrac{s}{k_n}\right) & (\text{otherwise}), \end{cases} \tag{4}$$

with $h_m = \beta_m l$, $k_n = n\pi l/L$, $s = (\omega + i\nu_{en})/(\sqrt{\omega^2+\nu_{en}^2})$, $\Lambda = (v_{\rm th}\omega_{pe}/c\omega)^2[1+(\nu_{en}/\omega)^2]^{-(3/2)}$ being system nonlocality, ω_{pe} being the electron plasma frequency, and Z_p being the plasma dispersion function.

Since the segmented coils are connected in parallel, the terminal voltages of the coils are equal to each other ($V_i = V_j \equiv V$). The sum of the coil currents is equal to the input current I from the impedance matching network ($I = \Sigma_{j=1}^{6} I_j$). Therefore we obtain for each i ($1 \leqslant i \leqslant 6$),

$$\sum_{j=1}^{6} [\mathcal{Z}_{ij} + \delta_{6i} Z_v]\gamma_j = Z \;\; \text{and} \;\; \sum_{j=1}^{6} \gamma_j = 1, \tag{5}$$

with $\gamma_j = I_j/I$ and $Z = V/I$ being the ratio of the jth coil current to the input total current and the total impedance of the system loaded to the matching network. Equation (5) determines the coil current ratios γ_j and the impedance of the system, Z, as functions of the processing parameters and external variable capacitance. Finally, the input current I can be determined from the relation $I = \sqrt{2P_{\rm rf}/R}\exp(i\Theta)$,[21] where the phase factor Θ depends on the impedance matching type and is given by $\Theta = \tan^{-1}(\sqrt{R_0/R-1})$ for the stan-

dard matching type[21] or $\Theta=\tan^{-1}[(X-W)/(R+XW/R)]$ for the alternate matching type[21] (these two impedance matching types are illustrated in Fig. 3). Here, R and X are the resistance and reactance of the system $(Z=R-iX)$, $W=\sqrt{(R^2+X^2-R_0R)R/R_0}$, $P_{\rm rf}$ is the rf-input power, and $R_0=50\,\Omega$ is the load resistance (see Fig. 3).

The inductive electric field may be obtained from the Maxwell–Boltzmann equations using the Fourier–Bessel transformation method;[18] the azimuthal inductive electric field E_θ and induced plasma current density J_p can be expanded in the Fourier–Bessel series without loss of generality as

$$E_\theta(r,z)=\sum_{m=1}^{\infty} J_1(p_m r)\left[\frac{e_{m0}}{2}+\sum_{n=1}^{\infty} e_{mn}\cos(q_n z)\right], \tag{6}$$

$$J_p(r,z)=\sum_{m=1}^{\infty} J_1(p_m r)\left[\frac{j_{m0}}{2}+\sum_{n=1}^{\infty} j_{mn}\cos(q_n z)\right]. \tag{7}$$

The Fourier–Bessel component of the inductive field e_{mn} is given by[18]

$$e_{mn}=\frac{2i\kappa l^2}{L}\left[1-(-1)^n\frac{\xi_{2m}}{\xi_{1m}}\right]\frac{b_{0m}}{D_{mn}}, \tag{8}$$

where b_{0m} is the Bessel component of the radial induced magnetic field at the plasma surface and has the following form:[21]

$$b_{0m}=\sum_{j=1}^{6}\frac{4\pi I_j}{cr_{\rm ch}^2}\frac{C_{mj}\sinh(\beta_m(z_j+L_s))\hat{b}_m}{\beta_m J_2^2(\alpha_{1m})\sinh(\beta_m L_s)}. \tag{9}$$

Under the assumption $\delta_s \ll r_{\rm ch}$ [where $\delta_s=(c^2 v_{\rm th}/\pi^{1/2}\omega\omega_{pe}^2)^{1/3}$ is anomalous skin depth[10]], the Fourier–Bessel component of the current density j_{mn} can be expressed as

$$j_{mn}=\sqrt{2\pi}\sigma_{q_n}e_{mn}, \tag{10}$$

where σ_{q_n} is the Fourier component of one-dimensional conductivity of infinite homogeneous plasmas[20] and given by

$$\sigma_{q_n}=\begin{cases}\dfrac{i}{4\pi\sqrt{2\pi}}\dfrac{\omega_{pe}^2}{(\omega+i\nu_{en})} & (\text{for } n=0),\\ -\dfrac{i}{4\pi\sqrt{2\pi}}\dfrac{\omega_{pe}^2}{q_n v_{\rm th}}Z_p\left(\dfrac{\omega+i\nu_{en}}{q_n v_{th}}\right) & (\text{otherwise}).\end{cases} \tag{11}$$

The power density absorbed by electrons is then given by

$$P_{\rm abs}=\tfrac{1}{2}\,{\rm Re}[J_p^* E_\theta]. \tag{12}$$

B. Plasma transport model

We now discuss the plasma transport model under fluid approximation. The basic equations consist of the drift-diffusion equations for ions and electrons, the diffusion equation for the neutral species, the electron temperature equation, and the Poisson equation,

$$\frac{\partial n_i}{\partial t}+\nabla\cdot\mathbf{\Gamma}_i=\sum_j k_{ij}^{iz}n_e N_j-\sum_{j,l}k_{jil}^r n_i n_l, \tag{13}$$

$$\frac{\partial n_e}{\partial t}+\nabla\cdot\mathbf{\Gamma}_e=\sum_{i,j}(k_{ij}^{iz}-k_{ij}^a)n_e N_j, \tag{14}$$

$$\frac{\partial N_j}{\partial t}+\nabla\cdot\mathbf{\Gamma}_{N,j}=\sum_l k_{jl}^d n_e N_l+\sum_{i,l}k_{jil}^r n_i n_l-\sum_i(k_{ij}^{iz}+k_{ij}^a)n_e N_j, \tag{15}$$

$$\mathbf{\Gamma}_i=\frac{1}{m_i\nu_i}[\alpha_i n_i\mathbf{E}-\nabla(n_i T_i)], \tag{16}$$

$$\mathbf{\Gamma}_e=\frac{1}{m_e\nu_e}[-n_e\mathbf{E}-\nabla(n_e T_e)], \tag{17}$$

$$\mathbf{\Gamma}_{N,j}=-\frac{T_N}{M_j\nu_{N,j}}\nabla(N_j T_N), \tag{18}$$

$$\frac{\partial T_e}{\partial t}+\nabla\cdot\left(\frac{T_e}{n_e}\mathbf{\Gamma}_e\right)-\frac{T_e}{3}\nabla\cdot\left(\frac{\mathbf{\Gamma}_e}{n_e}\right)=-\frac{2}{3n_e}\nabla\cdot\mathbf{q}_e+\frac{2P_e}{3n_e}, \tag{19}$$

$$\nabla^2\phi=-4\pi e\left(\sum_i \alpha_i n_i-n_e\right). \tag{20}$$

Here m_i, n_i, $\mathbf{\Gamma}_i$, and α_i are the mass, density, flux, and charge number of the ith ions, respectively. Similarly m_e, n_e, $\mathbf{\Gamma}_e$, T_e, $\mathbf{q}_e$, and P_e are the mass, density, flux, temperature, heat flux, and heat source of electrons, respectively, and M_j, N_j, and $\mathbf{\Gamma}_{N,j}$ are the mass, density, and flux of the jth neutral species, respectively. To obtain the particle production and loss rates by electron impact processes and/or heavy particle reactions, we take into account ionization, dissociation, attachment, and recombination processes, using reaction rate coefficients in the Arrhenius forms given in Ref. 12 for Ar discharges and Ref. 23 for Cl_2 discharges. Excited species and effects of etched products are not considered here for the sake of simplicity. The electron impact ionization, dissociation, and attachment reaction rate coefficients are denoted by k_{ij}^{iz}, k_{ij}^d, and k_{ij}^a, respectively, for jth neutral species to produce ith ions. The parameter k_{jil}^r is the recombination rate coefficient of ith ions with the lth ions to produce the jth neutral species. Also ν_i and ν_e are the collision frequencies of the ith ions and electrons, which are approximately equal to the ion–neutral and electron–neutral collision frequencies, ν_{in} and ν_{en}, for the weakly ionized gas (e.g., $\nu_{in}/\omega\sim 0.01 \gg \nu_{ii'}/\omega\sim 0.001$ and $\nu_{en}/\omega\sim 1\gg\nu_{ei}/\omega\sim 0.01$ in this simulation, where $\nu_{ii'}$ and ν_{ei} are the collision frequencies of ith ions and electrons with i'th ions and ith ions, respectively). The collision frequency between ions and neutral species is given as the sum of the elastic and charge exchange collision frequencies. We have used the Langevin scattering cross section,[24] $\sigma_L=(2\pi e/v_i)\sqrt{\alpha_p/m_R}$, and the resonant charge exchange collision cross section,[25] $\sigma_{\rm ex}=8\pi e^4/\epsilon_{iz}^2$, for the elastic and charge exchange collision frequencies, where v_i is the ion mean velocity, $m_R=m_i M_j/(m_i+M_j)$ is the reduced mass, and α_p and ϵ_{iz} are the polarizability and ionization energy of the neutral species, respectively. The collision frequency of the jth neutral species is denoted by $\nu_{N,j}$, which takes a value given by

either the particle–wall or particle–particle collision frequency, whichever is larger. We have also assumed ion and neutral temperatures, $T_i(=0.1\,\mathrm{eV})$ and $T_N(=0.026\,\mathrm{eV})$, to be constants. The electron heat flux $\mathbf{q}_e$ and heat source P_e are given by

$$\mathbf{q}_e = -\frac{5}{2}\frac{n_e T_e}{m_e \nu_{en}}\nabla T_e, \tag{21}$$

$$P_e = P_{\mathrm{abs}} - \sum_{i,j}\left[k_{ij}^{iz}(\epsilon_{ij}^{iz} + \tfrac{3}{2}T_e) + k_{ij}^{d}\epsilon_{ij}^{d} + k_{ij}^{a}(\epsilon_{ij}^{a} - \tfrac{3}{2}T_e)\right] n_e N_j, \tag{22}$$

where ϵ_{ij}^{iz}, ϵ_{ij}^{d}, and ϵ_{ij}^{a} are threshold energies for the ionization, dissociation, and attachment processes of jth neutral species to produce ith ions. Radiative power losses for the electrons have been ignored in this treatment.

We solve the fluid equations up to the plasma-sheath boundary (sheath edge) under the assumption that the particle fluxes are conserved within the sheath. This assumption is valid for the high density plasma sources operating at low pressures, because sheath thickness for them is very small (typically order of 0.1 mm) and collisions between particles within the sheath can be neglected. The boundary conditions at the sheath edge used in this model are as follows: the normal components of particle and heat fluxes on the boundary are given by

$$\Gamma_i = \begin{cases} \dfrac{\alpha_i n_i E}{m_i \nu_i} & \text{for positive ion} \\ 0 & \text{for negative ion} \end{cases}, \tag{23}$$

$$\Gamma_e = \tfrac{1}{4} n_e \exp(e\phi_w/T_e) v_e^{\mathrm{th}}, \tag{24}$$

$$\Gamma_{N,j} = \tfrac{1}{4}\eta_j N_j v_{N,j}^{\mathrm{th}} - \tfrac{1}{4}\xi_{jl} N_l v_{N,l}^{\mathrm{th}} - \Gamma_j, \tag{25}$$

$$q_e = e|\phi_w| T_e, \tag{26}$$

where η_j is the surface recombination probability for the jth neutral species, ξ_{jl} is the probability for the jth particle production by surface recombination of the lth neutral species, $v_e^{\mathrm{th}} = \sqrt{8T_e/\pi m_e}$, and $v_{N,j}^{\mathrm{th}} = \sqrt{8T_N/\pi M_j}$ are thermal velocities of the electron and jth neutral species, and ϕ_w is the sheath potential drop given by

$$\phi_w = -\frac{T_e}{e}\ln\left(\frac{n_e v_e^{\mathrm{th}}/4}{\Sigma_i n_i \sqrt{T_e/m_i}}\right). \tag{27}$$

Here the velocity of electrons and neutral species at the boundary, $v^{\mathrm{th}}/4$, comes from Maxwellian distribution assumption for their energy distribution. In deriving Eq. (27) we have used the ion velocity v_i at the sheath edge given by the following generalized Bohm criterion,[26]

$$\sum_i \frac{c_i}{\frac{1}{2}m_i v_i^2} \leqslant \frac{1}{T_e} \tag{28}$$

with $c_i = n_i/\Sigma_i n_i$, which is valid under the assumption that all the positive ions gain the same amount of energy from presheath.

To discretize the equations of motion, we have used the implicit finite difference method (FDM) on staggered uniform grids. To avoid the restriction on the maximum time step size due to the dielectric relaxation time, we have used the following equation in place of the Poisson equation:

$$\frac{\partial \mathbf{E}}{\partial t} + 4\pi\mathbf{J} = c\nabla\times\mathbf{B}, \tag{29}$$

where $\mathbf{E}$ is the electric field,

$$\mathbf{J} = e\left(\sum_i \alpha_i \mathbf{\Gamma}_i - \mathbf{\Gamma}_e\right) = \frac{\mathbf{E}}{4\pi\tau} - \sum_i \frac{e\alpha_i}{m_i\nu_{in}}\nabla(n_i T_i) + \frac{e}{m_e\nu_{en}}\nabla(n_e T_e) \tag{30}$$

is the plasma current density induced by the electric field and by particle diffusion, and $\tau = [\omega_{p,e}^2/\nu_{en} + \Sigma_i(\omega_{p,i}^2/\nu_{in})]^{-1}$ is the dielectric relaxation time. Since $|\partial\mathbf{E}/\partial t| \sim \mathbf{E}/\tau$, $c|\nabla\times\mathbf{B}| \sim (\tau c^2/L^2)\mathbf{E}$, and $1/\tau(\sim 10^{13}\,\mathrm{Hz}) \gg \tau c^2/L^2(\sim 10^6\,\mathrm{Hz})$, we may simplify Eq. (29) by neglecting the right-hand side. Equations (29) and (30) are then combined to give

$$\frac{\partial \mathbf{E}}{\partial t} + \frac{\mathbf{E}}{\tau} = \sum_i \frac{e\alpha_i}{m_i\nu_{in}}\nabla(n_i T_i) - \frac{e}{m_e\nu_{en}}\nabla(n_e T_e). \tag{31}$$

If we assume that the right-hand side in Eq. (31) is constant during time step Δt, the solution of Eq. (31) may be given by

$$\mathbf{E}(t+\Delta t) = 4\pi\tau\mathbf{J}\left[\exp\left(-\frac{\Delta t}{\tau}\right) - 1\right] + \mathbf{E}(t). \tag{32}$$

Equation (32) clearly indicates that the numerical instability can occur if the time step is taken to be larger than the dielectric relaxation time; if we applied the FDM for the discretization in time without the above consideration, Eq. (32) could be replaced by

$$\mathbf{E}(t+\Delta t) = -4\pi\Delta t\mathbf{J} + \mathbf{E}(t), \tag{33}$$

which will not yield the same result if $\Delta t \gg \tau$. Thus, Eq. (32) must be used when $\Delta t \gg \tau$.

The Peclet number is the ratio of the strength of convection to that of diffusion and may be defined by $\varepsilon_z \Delta z/T$ or $\varepsilon_r \Delta r/T$, where $\varepsilon = \mathbf{E} - \nabla T$ with T being T_i for ions and T_e for electrons. It is known that if the Peclet number is greater than unity,[27,28] the straightforward discretization of Eqs. (16) and (17) by the FDM can cause numerically instability. In our simulations, the Peclet number can be often larger than unity near the sheath region, where we have used a power-law scheme, instead of the simple FDM, to approximate the exponential scheme.[28] The radial and axial components of the particle flux at midpoints between the neighboring grid nodes in the exponential scheme are given by

$$\Gamma_r^{i+(1/2),k} = d_r^{i+(1/2),k}(b_r^{i+(1/2),k} n_{i,k} - a_r^{i+(1/2),k} n_{i+1,k}), \tag{34}$$

$$\Gamma_z^{i,k+(1/2)} = d_z^{i,k+(1/2)}(b_z^{i,k+(/2)} n_{i,k} - a_z^{i,k+(1/2)} n_{i,k+1}), \tag{35}$$

where $d_x \equiv T/M\nu\Delta x$, $b_x \equiv P_x \exp(P_x)/\exp(P_x) - 1$, $a_x \equiv P_x/\exp(P_x) - 1$, and $P_x \equiv \epsilon_x \Delta x/T$. Here $x = r$ or z, and i and k are radial and axial grid numbers, respectively. This exponential scheme guarantees the exact solution for any

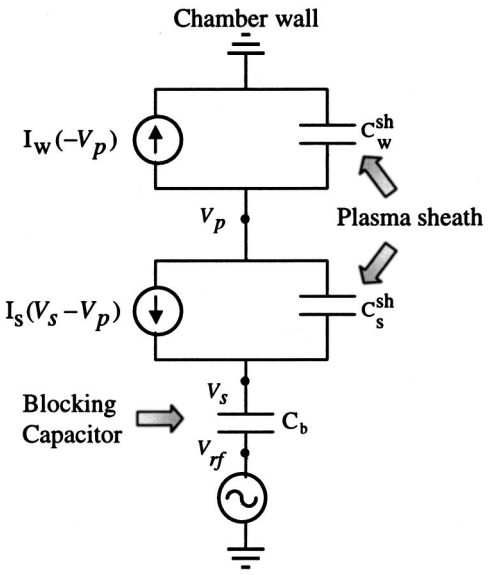

FIG. 4. Schematic diagram of the equivalent circuit for our dc-bias model.

value of the Peclet number. However the exponential scheme is not widely used because exponential functions are relatively slow to evaluate numerically. We therefore adopt the power-law scheme which provides fairly good representation of the exponential scheme and can be easily evaluated numerically. In the power law scheme,[28] for any value of the Peclet number P, the functions a and b in Eqs. (34) and (35) can be given as

$$a(P)=\mathrm{Max}[0,(1-0.1|P|)^5]+\mathrm{Max}[-P,0], \tag{36}$$

$$b(P)=\mathrm{Max}[0,(1-0.1|P|)^5]+\mathrm{Max}[P,0], \tag{37}$$

for both r and z components.

Deviation from charge neutrality, $\rho=\Sigma_i \alpha_i n_i - n_e$, is accounted for by redistributing the space charge to each species in proportion to the amount of its charge in the plasma after each time step as follows:

$$n_i \rightarrow n_i - \frac{\alpha_i n_i/|\alpha_i|}{\Sigma_i |\alpha_i| n_i + n_e}\rho, \tag{38}$$

$$n_e \rightarrow n_e + \frac{n_e}{\Sigma_i |\alpha_i| n_i + n_e}\rho. \tag{39}$$

The initial values for the electrostatic field, ion fluxes, and ϕ_w are set to be zero and that for the electron flux at the wall is given by Eq. (24). As the simulation progresses, the electrostatic fields and ϕ_w are evolved to nullify the net current density and to force the ion to reach the Bohm velocity at the sheath boundary.

C. Model for poly-Si etch profile evolution

The etch profile simulation module computes the bias voltage, ion flux distribution (IFD) on the substrate, etch rate, and profile evolution, as shown in Fig. 2. Separate models for these calculations are described below.

To determine the bias voltage self-consistently, we use a circuit model described schematically in Fig. 4. Here the sheaths on the chamber wall and biased substrate are assumed to be capacitors connected in series through the plasma, neglecting capacitance between the antenna and plasma ($c_{sh}/c_{ap} \sim l_d/l_{sh} \gg 1$, where c_{sh} and c_{ap} are sheath and antenna-plasma capacitances per unit area, respectively, and $l_d \sim 1$ cm and $l_{sh} \sim 0.1$ mm are dielectric window and sheath thicknesses, respectively). Using the rf-sheath model in Ref. 29, we obtain the following relations:

$$C_s^{sh}\frac{d}{dt}(V_p - V_s) + C_b \frac{d}{dt}(V_{rf} - V_s) + I_s = 0, \tag{40}$$

$$C_w^{sh}\frac{d}{dt}V_p + C_s^{sh}\frac{d}{dt}(V_p - V_s) + I_s + I_w = 0, \tag{41}$$

where C_s^{sh} and C_w^{sh} are the sheath capacitances on the substrate and chamber wall, C_b is the blocking capacitance, V_p, V_s, and V_{rf} are the plasma potential, substrate voltage, and rf input voltage, respectively, I_s and I_w are the conduction currents into the substrate and chamber wall. The sheath capacitance C^{sh} is related with the voltage drop $V_{sh}=V_s-V_p$ across the sheath as[29]

$$C^{sh} = -\frac{S}{4\pi}\frac{\partial E_S}{\partial V_{sh}}, \tag{42}$$

where $E_S = -(8\pi T_e n_e)^{1/2}[\exp(e(V_{sh}-V_1)/T_e) + (V_{sh}/V_1)^{1/2} - 2]^{1/2}$ is the electric field at the electrode surface, S is the surface area, and $V_1 = -(T_e/2e)$ denotes the potential drop in the presheath. The conduction current $I(V_{sh})$ into the sheath (as a function of the sheath voltage V_{sh}) is given by

$$I(V_{sh}) = eS\left[\sum_i \alpha_i \Gamma_i - \Gamma_e \exp(eV_{sh}/T_e)\right], \tag{43}$$

where Γ_i and Γ_e are fluxes of the ith ion species and electrons normal to the sheath edge, which may be determined from the fluid model. Here we neglect the negative ions because their density at the sheath edge is nearly zero due to their low temperature [the Boltzmann factor, $\exp(-eV_p/T_i) \lesssim 10^{-43}$ in this simulation]. The nonlinearly coupled Eqs. (40) and (41) can be solved by the Runge–Kutta method.

In order to obtain the incident ion flux distribution across the sheath, we have employed a particle simulation similar to that given in Refs. 30 and 31. In the simulation, a statistically meaningful number of ions (50 000) are introduced at the sheath boundary with the Bohm velocity and their equations of motion are solved in an electric field given by the Child–Langmuir Law,

$$E_y(t,y) = -\frac{4V_{sh}(t)}{3l_{sh}}\left(\frac{y}{l_{sh}}\right)^{1/3}, \tag{44}$$

with l_{sh} and y being the sheath thickness and the axial position from the sheath edge.

Using the ion energy distribution on the substrate, we calculate the etch rate at each location on a trench surface. In the case of ion-enhanced poly-Si etching case, the etch rate (ER) may be given by[32]

$$\mathrm{ER} = \frac{1}{\rho_{Si}}\theta \sum_i \int_{-\Phi_1}^{\Phi_2} Y_{Si}^i(\Phi)\ \Gamma_i d\Phi, \tag{45}$$

where $\rho_{Si}(=5.0\times10^{22}\,\mathrm{cm}^{-3})$ is the atomic density of poly-Si substrate, θ is the surface coverage by Cl on the Si surface, $-\Phi_1$ and Φ_2 are the minimum and maximum incident angles which limit the trajectory of the ion by shadowing effects of the mask edge, $Y^i_{Si}(\Phi)$ is the etch yield for the ith ions with incident angle Φ, and Γ_i is the flux of the ith ions incident on the Si surface. In what follows, the dependence of the etch yield on the incident angle is assumed as $Y^i_{Si}(\Phi)=Y^i_{Si}(0)\cos^{1/2}\Phi$,[32] which is appropriate for this simulation because the limits on the integral in Eq. (45), Φ_1 and Φ_2, are less than about 50° for our mask geometry.

The surface coverage θ can be determined from the flux balance of neutral reactants on the Si surface and given by

$$\theta=\frac{S_{n0}\Gamma_N}{S_{n0}\Gamma_N+Y_{Cl}\Sigma_i\Gamma_i}. \tag{46}$$

Here S_{n0} is the sticking probability on the bare surface and 0.99 for neutral Cl,[33] and Y_{Cl} is the number of Cl atoms per incident ion and given by 3.[32] Since we have observed in our simulation that the typical ratio of the Cl flux to Cl_2 flux on the substrate is about 4.2 and the sticking probability of Cl atoms is about two times higher than that of Cl_2 molecules, we neglect reactions involving Cl_2 and assume Γ_N to be the Cl flux only. Unlike ions, however, neutral reactants reach the substrate surface with an isotropic angular distribution, and experience adsorption and re-emission processes. In other words, the incident neutral flux consists of the directly incident neutrals from the plasma and re-emitted neutrals from other locations of the surface structure (such as trench walls) and therefore Γ_N is then a function of θ, too. To determine Γ_N, we have used the iteration method given in Ref. 32.

The etch yield $Y^i_{Si}(\Phi=0)$ for normal incident ions is known to linearly depend on the square root of the incident ion energy E_{ion},[34–36] i.e., $A(E^{1/2}_{ion}-E^{1/2}_{th})$, where A and E_{th} are constants that depend on the species[35] and the ratio of neutral to ion fluxs.[35,37] Chang and Sawin[35] measured the ion-enhanced etch yield for Cl^+ ions with background Cl or Cl_2 and observed that the etch yield increases sharply at low neutral-to-ion flux ratios (i.e., the neutral-limited regime) but gradually saturates at high flux ratios (i.e., the ion-limited regime). Levinson *et al.*[37] reported similar results for etching by Ar^+/Cl_2. In our simulations presented in the next section, the minimum ratio of neutral to ion fluxes on the substrate is beyond 100 and therefore the etching processes are in the ion-limited regime. In this regime, experimental data in Refs. 35 and 36 are available for etching by $Cl^+/(Cl\ \text{or}\ Cl_2)$ and Cl_2^+/Cl_2, respectively. However, to the best of our knowledge, there is no available experimental data for etching by Cl_2^+/Cl in the ion-limited regime. The effect of Cl and Cl_2 on etch yield in the presence of Cl^+ has been investigated in Ref. 35; the etch yield by Cl^+/Cl_2 is two times smaller than that by Cl^+/Cl in the ion-limited regime, because the dissociative adsorption of molecular chlorine is limited in the high neutral flux regime where the silicon surface is highly chlorinated. Based on this study, we therefore assume that the etch yield by Cl_2^+/Cl is two times higher than that by Cl_2^+/Cl_2 given in Ref. 36. Thus we use the following etch yield functions in simulations presented below:

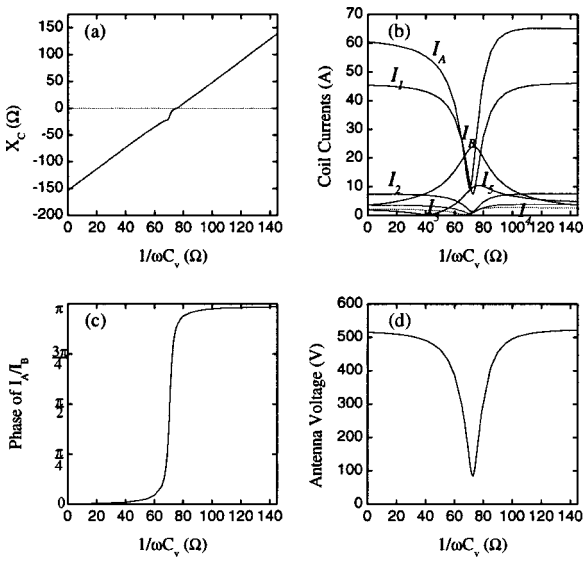

FIG. 5. Dependence of (a) reactance of the circuit C in Fig. 1(b), (b) magnitudes of the coil currents, (c) phase difference between I_A and I_B, and (d) terminal voltage of the antenna on the reactance of the external variable capacitor C_v for Ar discharges with 500 W rf power and 10 mTorr gas pressure.

$$Y^{Cl^+}_{Si}(0)=0.909E^{1/2}_{ion}-4.318 \quad (\text{for etching by } Cl^+/Cl), \tag{47}$$

$$Y^{Cl_2^+}_{Si}(0)=0.435E^{1/2}_{ion}-2.174 \quad (\text{for etching by } Cl_2^+/Cl). \tag{48}$$

We now briefly discuss the simulation method for etch profile evolution. Suppose $F(\mathbf{x},t)=0$ represents the interface during etching processes, the interface evolution equation may be given by

$$\frac{\partial F}{\partial t}+k\mathbf{Q}_i\cdot\nabla F=0, \tag{49}$$

with $k=\mathrm{ER}/(\hat{n}\cdot\mathbf{Q}_i)$. Here $\hat{n}=\nabla F/|\nabla F|$ is the unit vector normal to the interface, and $\mathbf{Q}_i$ is the ion energy flux at a surface position (x,y). If the profile is such that one can write $F(x,y,t)=y-\eta(x,t)$ [i.e., the height of the profile $\eta(x,t)$ is a function of x], then Eq. (49) becomes

$$\frac{\partial\eta}{\partial t}+kQ_{i,x}(\eta,x)\frac{\partial\eta}{\partial y}=kQ_{i,y}(\eta,x). \tag{50}$$

The characteristic equations of the above partial differential equation are then given by

$$\frac{dx}{dt}=kQ_{i,x}(\eta,x), \tag{51}$$

$$\frac{d\eta}{dt}=kQ_{i,y}(\eta,x). \tag{52}$$

We have numerically solved Eqs. (51) and (52),[38,39] using the poly-Si etch rate formula Eq. (45) and particle simulation results for the energy distributions of ion flux.

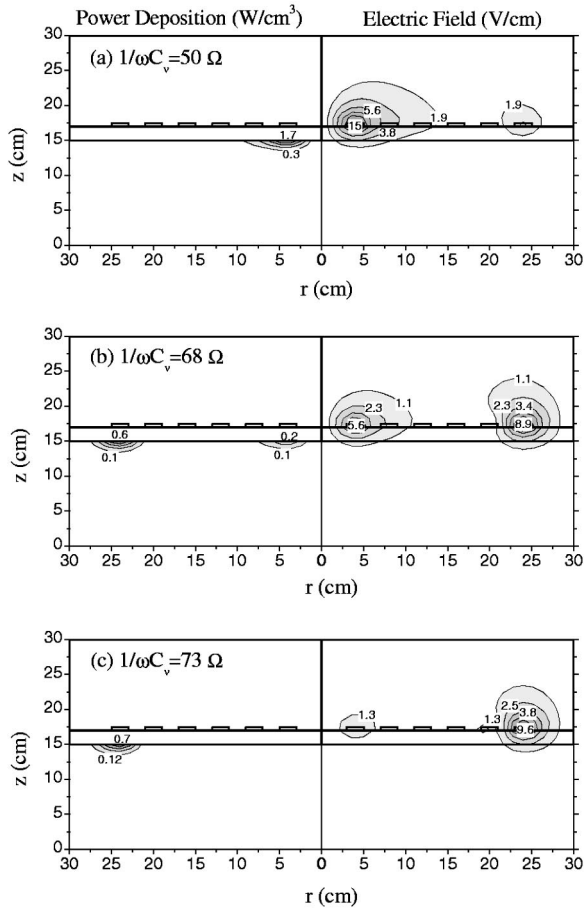

FIG. 6. Profiles of the power deposition and amplitude of inductive electric fields for Ar discharges with 500 W rf power and 10 mTorr gas pressure, where $1/\omega C_v$ is (a) 50 Ω, (b) 68 Ω, and (c) 73 Ω.

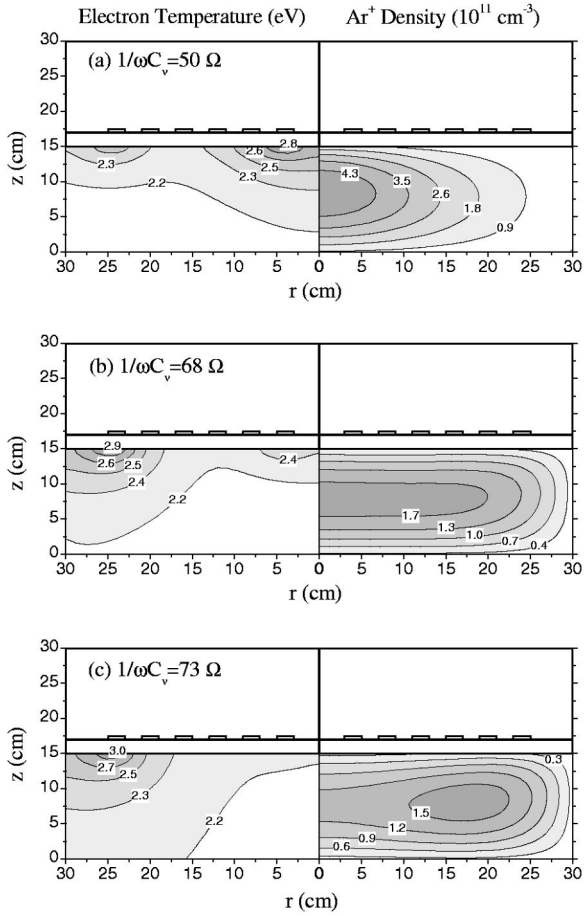

FIG. 7. Electron temperature and Ar^+ ion density profiles for Ar discharges. The discharge conditions are the same as those given in Fig. 6.

IV. RESULTS AND DISCUSSION

Simulations were performed for Ar and Cl_2 discharges with 10 mTorr gas pressure. The input rf powers are 500 W for Ar discharges and 1.5 kW for Cl_2 discharges. The geometric parameters are as follows: the chamber radius r_{ch} is 30 cm, the chamber length L is 15 cm, the shielding cap length L_s is 15 cm, the thickness of dielectric window is 2 cm, the substrate radius is 25 cm, the coil thickness and width are 0.2 cm and 2 cm, and the radial positions of 6 antenna coils are 4, 8, 12, 16, 20, and 24 cm. Resistivity of $5.33\times10^{-3}\,\Omega$ cm (i.e., the resistivity of Cu) is used to calculate the coil resistance R_{ci}.

Figure 5 shows various characteristics of the antenna as functions of the external variable capacitance C_v. Figure 5(a) shows the dependence of the reactance of circuit element C of Fig. 1(b), i.e., $X_C=X_A+X_B$, on the impedance of the external variable capacitance of $Z_v=i/\omega C_v$. Here $X_A=\mathrm{Im}(\Sigma_{i=1}^{5}Z_i^{-1})^{-1}$ and $X_B=\mathrm{Im}(Z_6+Z_v)$ are the reactances of circuit elements A and B of Fig. 1(b) and $Z_i=\Sigma_{j=1}^{6}I_i^{-1}\mathcal{Z}_{ij}I_j$ is the impedance of the ith coil. Figure 5(b) shows the coil currents as functions of Z_v. Figures 5(c) and 5(d) show the dependence of the phase of I_A/I_B and the antenna terminal voltage V on Z_v. As can be seen from Figs. 5(a), 5(b), and 5(c), the LC-resonance occurs in the circuit C near $X_C=0$, where $I_A=\Sigma_{j=1}^{5}I_j$ and $I_B=I_6$ are nearly the same in magnitude but in the opposite direction. As a result, a resonance peak appears in the current of the sixth coil at $1/\omega C_v=73\,\Omega$. Since the increase of the sixth coil current means the increase of plasma generation in the peripheral region, we expect that the radial plasma density profile may be optimized by adjusting C_v. Near the resonance conditions, the total input antenna current $I=I_A+I_B$ decreases, resulting in very small antenna voltage V, as shown in Fig. 5(d).

Figures 6 and 7 present the fluid simulation results of Ar discharges for three cases: (a) off-resonant case ($1/\omega C_v=50\,\Omega$), (b) optimum case ($1/\omega C_v=68\,\Omega$), and (c) resonant case ($1/\omega C_v=73\,\Omega$). Figure 6 shows the power deposition and inductive electric field profiles. In the off-resonant case ($1/\omega C_v=50\,\Omega$), small reactances of the inner coils induce large currents, causing large electric fields and power deposition in the inner region, as shown in Fig. 6(a). However, as C_v approaches the LC-resonance value, the outer most coil current I_B increases up to the sum of the other coil currents and the electric fields and power deposition in the outer region also increases, as shown in Figs. 5(b) and 5(c).

Figure 7 shows the electron temperature and Ar^+ ion density profiles as functions of $1/\omega C_v$. The power deposition for the off-resonant case in Fig. 6(a) yields the centrally peaked profiles of the electron temperature and Ar^+ density in Fig. 7(a). As C_v approaches the LC-resonance value, the

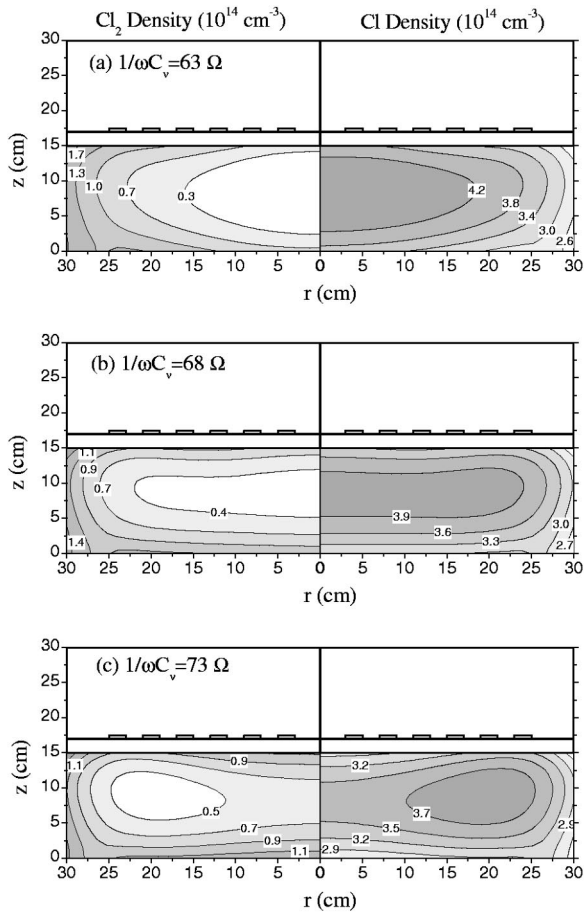

FIG. 8. Cl_2 and Cl neutral density profiles for Cl_2 discharges with 1.5 kW rf power and 10 mTorr gas pressure, where $1/\omega C_v$ is (a) 63 Ω, (b) 68 Ω, and (c) 73 Ω.

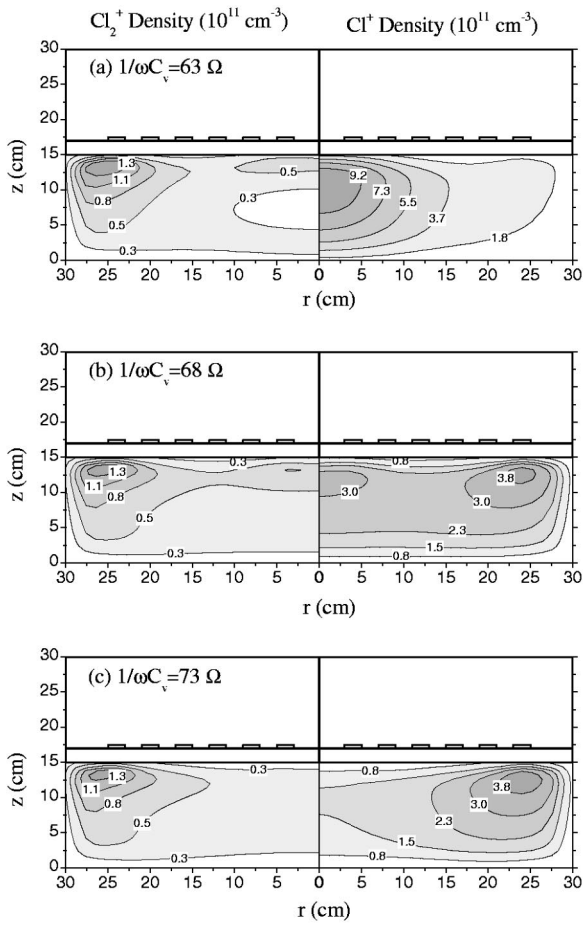

FIG. 9. Cl_2^+ and Cl^+ ion density profiles for Cl_2 discharges. The discharge conditions are the same as those given in Fig. 8.

electron temperature and power deposition in the outer region increases and the plasma profile extends radially, as shown in Figs. 7(b) and 7(c). When $1/\omega C_v = 68\,\Omega$ the radial spread of the plasma on the substrate becomes optimized and uniform within 2% over 300 mm in diameter.

In the case of Cl_2 discharges (which is not presented here), electric characteristics of the antenna coils are nearly the same as those shown in Fig. 5. This is because reactances of the coil segments are mainly determined by their geometric configurations. In Figs. 8 and 9, the Cl_2 plasma density profiles are plotted for (a) off resonant $1/\omega C_v = 63\Omega$, (b) optimum $1/\omega C_v = 68\Omega$, and (c) resonant $1/\omega C_v = 73\Omega$. Figure 8 shows the density profiles of neutral Cl atoms and Cl_2 molecules. Here we observe a depletion region of Cl_2 due to the dissociation to Cl atoms. The depletion region moves toward the outer region as $1/\omega C_v$ approaches to the resonance value. Figure 9 shows the density profiles of Cl^+ and Cl_2^+ ions. Since the Cl^+ ion is mainly produced by direct ionization of Cl, its density profiles with various external capacitances resemble those of Ar^+ given in Fig. 7. However, due to the lack of neutral Cl_2 molecules in the depletion region, the Cl_2^+ density profile is insensitive to change of the variable capacitance C_v.

Figure 10 presents radial profiles of the total ion flux, i.e., sum of Cl^+ and Cl_2^+ ion fluxes, onto the substrate for various C_v. For the optimum case ($1/\omega C_v = 68\,\Omega$), the ion flux is uniform within 2.3% over 300 mm in diameter.

Figure 11 shows time dependence of the sheath voltage for various C_v when the applied voltage and frequency on the electrode are set to be 80 V and 13.56 MHz, and the blocking capacitance is 5000 pF. It shows a distorted sinusoidal form due to the nonlinear characteristics of the sheath.

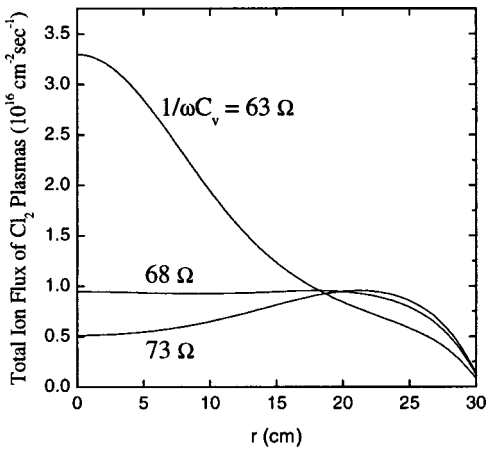

FIG. 10. Radial profiles of the total ion fluxes onto the substrate for Cl_2 discharges for various external capacitances. Here the rf power is 1.5 kW and the gas pressure is 10 mTorr.

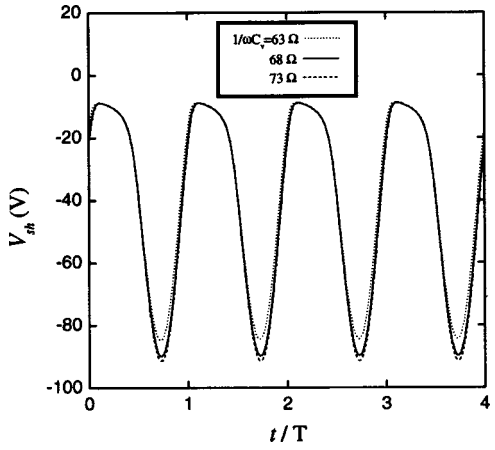

FIG. 11. Time dependence of the sheath voltage between the electrode and plasma for various external capacitances for Cl_2 discharges condition with 1.5 kW rf power and 10 mTorr gas pressure. The applied voltage and frequency on the electrode are 80 V and 13.56 MHz and the blocking capacitance is 5000 pF. The time is normalized by the rf period T.

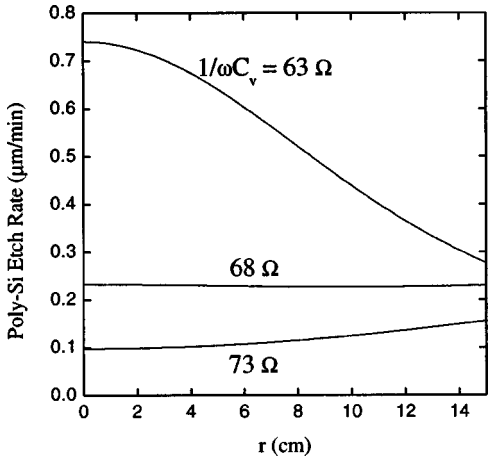

FIG. 13. Radial profiles of the poly-Si etch rates for various external capacitances. Here the rf power is 1.5 kW and the Cl_2 gas pressure is 10 mTorr.

The time averaged dc bias voltages V_{dc}, which come from the the mobility difference between electrons and ions, are -38, -41, and -42 V for $1/\omega C_v = 63$, 68, and 73 Ω, respectively.

Figure 12 presents the Cl^+ and Cl_2^+ ion fluxes onto the substrate as functions of the ion kinetic energy for various external capacitances under the time-varying sheath voltages given in Fig. 11. The energy distribution is normalized to enclose a unit area and the kinetic energy K is normalized by the average kinetic energy $\langle K\rangle = \int K\Gamma_i(K)dK / \int \Gamma_i(K)dK$, whose values are 48.7, 53.6, and 45.6 eV for Cl^+, and 52.3, 41.1, and 41.7 eV for Cl_2^+, when $1/\omega C_v = 63$, 68, and 73 Ω, respectively. The energy spread widths in Fig. 12 are in good

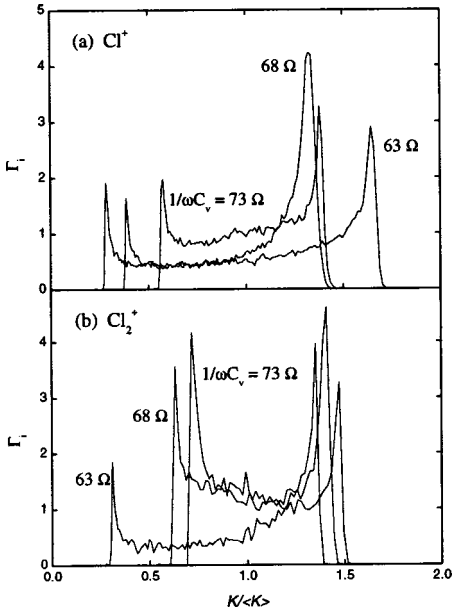

FIG. 12. Dependence of (a) Cl^+ and (b) Cl_2^+ ion fluxes onto the substrate on the kinetic energy K for various external capacitances. The energy distributions are normalized to enclose a unit area and the energy is normalized by the average kinetic energy $\langle K\rangle$.

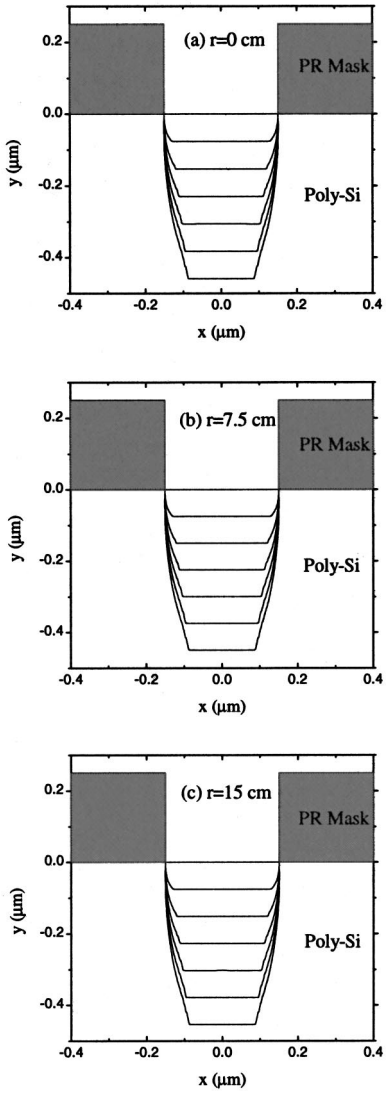

FIG. 14. Temporal evolution of poly-Si etch profiles in the optimum case of Fig. 13 ($1/\omega C_v = 68\ \Omega$) for 2 min at three different positions on the 300 mm wafer: (a) $r = 0$ cm (center), (b) $r = 7.5$ cm (middle), and (c) $r = 15$ cm (edge).

agreement with the analytic formula in Ref. 40, i.e., $\Delta K = 2eE_1/\omega(-2eV_{dc}/m_i)^{1/2}$, where $E_1 = 4V_{sh}^{pp}/3l_{sh}$ is the amplitude of oscillating part of the electric field at the electrode and V_{sh}^{pp} is peak-to-peak value of the sheath voltage. The energy spread ΔK obtained in our numerical simulations agrees with the analytical value within 8% error.

Figure 13 shows radial profiles of the poly-Si etch rates for various external capacitances, which are obtained from Eq. (45) using the ion flux distributions in Fig. 12. We observe that etch uniformity can be controlled by adjusting the external variable capacitor, resulting in the optimized rate variation of less than 2.5% over 300 mm in diameter when $1/\omega C_v = 68\,\Omega$. In Fig. 14, microscopic etched structures are compared at three different positions (from the center to edge) on a 300 mm wafer when $1/\omega C_v = 68\,\Omega$. The temporal evolutions of etch profiles during 2 min are also shown to be uniform over the 300 mm wafer diameter.

V. CONCLUDING REMARK

A self-consistent model and numerical simulation codes based on the model have been developed to investigate electron heating, plasma transport, and etching characteristics in the large-area resonant ICP (RICP) source. Our simulation results indicate that a properly tuned six-segmented coil system with an external variable capacitor allows the source to produce uniform large-area plasmas suitable for uniform poly-Si etching processes on 300 mm wafers. The controllability of plasma and etching uniformity of this device is attributed to the LC-resonance induced in the coil system. The plasma density profile in the radial direction becomes flatter as the reactance of the external capacitor approaches the LC-resonance condition and is optimized for uniform etching over large area at some value of the external capacitance near the resonance condition. Although we have considered only six-segmented coils in the present study, the same resonance method is applicable to any number of coil segments.

ACKNOWLEDGMENTS

The work of S. S. Kim was supported by the Korea Science and Engineering Foundation fellowship and that of S. Hamaguchi was supported in part by the Kawasaki 21st Century Foundation. This work was also supported in part by the Korea Ministry of Science and Technology and the Korea Ministry of Commerce, Industry and Energy under System IC project contract.

[1] V. Singh and J. Holland, IEEE Trans. Plasma Sci. **24**, 133 (1996).
[2] Y. Wu and M. A. Lieberman, Appl. Phys. Lett. **72**, 777 (1998).
[3] N. Sato, S. Iizuka, Y. Nakagawa, and T. Tsukada, Appl. Phys. Lett. **62**, 1469 (1993).
[4] Y. Li, S. Iizuka, and N. Sato, Appl. Phys. Lett. **65**, 28 (1994).
[5] S. Samukawa, Y. Nakagawa, T. Tsukada, and H. Ueyama, Jpn. J. Appl. Phys. **34**, 6805 (1995).
[6] S. S. Kim, H. Y. Chang, C. S. Chang, and N. S. Yoon, Appl. Phys. Lett. **77**, 492 (2000).
[7] J. Hopwood, C. R. Guarnier, S. J. Whitehair, and J. J. Cuomo, J. Vac. Sci. Technol. A **11**, 152 (1993).
[8] J. H. Keller, J. C. Foster, and M. S. Barnes, J. Vac. Sci. Technol. A **11**, 2487 (1993).
[9] J. A. Meyer and A. E. Wendt, J. Appl. Phys. **78**, 1 (1995).
[10] M. M. Turner, Phys. Rev. Lett. **71**, 1844 (1993).
[11] V. A. Godyak, R. B. Piejak, and B. M. Alexandrovich, Plasma Sources Sci. Technol. **3**, 169 (1994).
[12] R. A. Stewart, P. Vitello, and D. B. Graves, J. Vac. Sci. Technol. B **12**, 478 (1994).
[13] A. P. Paranjpe, J. Vac. Sci. Technol. A **12**, 1221 (1994).
[14] P. L. G. Ventzek, T. J. Sommerer, R. J. Hoekstra, and M. J. Kushner, Appl. Phys. Lett. **63**, 605 (1993).
[15] P. L. G. Ventzek, M. G. Grapperhaus, and M. J. Kushner, J. Vac. Sci. Technol. B **12**, 3118 (1994).
[16] V. Vahedi, M. A. Lieberman, G. DiPeso, T. D. Rognlien, and D. W. Hewett, J. Appl. Phys. **78**, 1446 (1995).
[17] R. S. Wise, D. P. Lymberopoulos, and D. J. Economou, Appl. Phys. Lett. **68**, 2499 (1996).
[18] N. S. Yoon, S. M. Hwang, and D. I. Choi, Phys. Rev. E **55**, 7536 (1997).
[19] M. S. Barnes, J. C. Foster, and J. H. Keller, Appl. Phys. Lett. **62**, 2622 (1993).
[20] N. S. Yoon, S. S. Kim, C. S. Chang, and D. I. Choi, Phys. Rev. E **54**, 757 (1996).
[21] N. S. Yoon and S. S. Kim, ''Impedance calculation of planar-type inductively coupled plasma discharges,'' Phys. Rev. E (to be submitted).
[22] J. D. Jackson, *Classical Electrodynamics* (Wiley, New York, 1975), pp. 242, 243.
[23] E. Meeks and J. W. Shon, IEEE Trans. Plasma Sci. **23**, 539 (1995).
[24] M. A. Lieberman and A. J. Lichtenberg, *Principles of Plasma Discharges and Materials Processing* (Wiley, New York, 1994), p. 62.
[25] V. E. Golant, A. P. Zhilinsky, I. E. Sakharov, and S. C. Brown, *Fundamentals of Plasma Physics* (Wiley, New York, 1977).
[26] K.-U. Rieman, J. Phys. D **24**, 493 (1991).
[27] Y. H. Oh, N. H. Choi, and D. I. Choi, J. Appl. Phys. **67**, 3264 (1990).
[28] S. V. Patankar, *Numerical Heat Transfer and Fluid Flow* (McGraw–Hill, New York, 1980).
[29] A. Metze, D. W. Errie, and H. J. Oskam, J. Appl. Phys. **60**, 3081 (1986).
[30] Y. D. Lee, S. S. Kim, S. H. Ku, and C. S. Chang, Phys. Plasmas **7**, 766 (2000).
[31] J. Ignacio, F. Ulacia, and J. P. McVittie, J. Appl. Phys. **65**, 1484 (1989).
[32] M. Tuda, K. Nishikawa, and K. Ono, J. Appl. Phys. **81**, 960 (1997).
[33] R. J. Hoekstra, M. J. Grapperhaus, and M. J. Kushner, J. Vac. Sci. Technol. A **15**, 1913 (1997).
[34] C. Steinbrüchel, Appl. Phys. Lett. **55**, 1960 (1989).
[35] J. P. Chang and H. H. Sawin, J. Vac. Sci. Technol. A **15**, 610 (1997).
[36] M. Balooch, M. Moalem, W.-E. Wang, and A. V. Hamza, J. Vac. Sci. Technol. A **14**, 229 (1996).
[37] J. A. Levinson, E. S. G. Shaqfeh, M. Balooch, and A. V. Hamza, J. Vac. Sci. Technol. A **15**, 1902 (1997).
[38] E. S. G. Shaqfeh and C. W. Jurgensen, J. Appl. Phys. **66**, 4664 (1989).
[39] S. Hamaguchi, M. Dalvie, R. T. Farouki, and S. Sethuraman, J. Appl. Phys. **74**, 5172 (1993).
[40] S. Hamaguchi, R. T. Farouki, and M. Dalvie, Phys. Rev. Lett. **68**, 44 (1992).